ISSN 0030-400X, Optics and Spectroscopy, 2013, Vol. 114, No. 4, pp. 525–536. © Pleiades Publishing, Ltd., 2013.

CONDENSED-MATTER SPECTROSCOPY

FT-IR, FT-Raman, NMR Spectra and DFT Simulations of 4-(4-Fluoro-phenyl)-1H-imidazole[1]

Y. Erdogdu[b], D. Manimaran[b], M. T. Güllüoğlu[a], M. Amalanathan[b], I. Hubert Joe[b], and Ş. Yurdakul[c]

[a] *Department of Physics, Ahi Evran University, 40040 Kirsehir, Turkey*

[b] *Department of Physics, Centre for Molecular and Biophysics Research, Mar Ivanios College, Thiruvananthapuram-695 015, Kerala, India*

[c] *Department of Physics, Gazi University, 06500 Ankara, Turkey*

e-mail: yusuferdogdu@gmail.com

Received July 19, 2012

Abstract—The FT-IR, FT-Raman and FT-NMR spectra of the compound 4-(4-Fluoro-phenyl)-1H-imidazole (4-FPI) were recorded and analyzed. Density functional method (B3LYP level with the 6-311G(d, p) and 6-311++G(d, p) and cc-pVQZ as basis sets) has been used to compute optimized geometry, vibrational wavenumbers of the 4-FPI. Only one tautomeric form was found most stable by using DFT/B3LYP. The detailed interpretation of the vibrational spectra was carried out with the aid of total energy distribution following the scaled quantum mechanical force field methodology. Potential Energy Surface scan studies has also been carried out by ab initio calculations with the same basis sets.

DOI: 10.1134/S0030400X13040073

INTRODUCTION

Imidazole is a heterocyclic compound of five-membered diunsaturated ring structure composed of three carbon atoms and two nitrogen atoms at nonadjacent positions. Imidazole ring is found in histidine (an essential amino acid) and in histamine, the decarboxylated compound from histamine. Some imidazole compounds inhibit the biosynthesis of ergo sterol, required in cell membrane in fungal. They have antibacterial, antifungal, antiprotozoal, and anthelmintic activity. Imidazole and its derivatives are widely used as intermediates in synthesis of organic target compounds including pharmaceuticals, agrochemicals, dyes, photographic chemicals, corrosion inhibitors, epoxy curing agents, adhesives and plastic modifiers [1, 2]. The phenylimidazole molecular fragment plays a primary role in the functional architecture of biologically active molecules such as novel histamine H_2 receptor antagonists [3], cardio tropic agents [4] and several types of artificial enzymes [5–8].

FT-IR, FT-Raman and FT-NMR spectra of 4-phenylimidazole molecule using theoretical and experimental methods have been reported earlier [9]. The present paper deals with the Infrared, Raman and NMR spectra of 4-(4-Fluoro-phenyl)-1H-imidazole (4-FPI) molecule along with the theoretical prediction using DFT method. The change in electron density (E_D) in the σ* antibonding orbitals and $E(2)$ energies have been calculated by natural bond orbital analysis.

[1] The article is published in the original.

EXPERIMENTAL

The title compound 4-FPI (99% Aldrich) was purchased from Sigma-Aldrich and used without further purification. The FT-IR spectrum of this molecule is recorded in the region 4000–400 cm^{-1} on IFS 66V spectrophotometer using KBr pellet technique. The FT-Raman spectrum of 4-FPI has been recorded using 1064 nm line of Nd:YAG laser as excitation wavelength in the region 50–3500 cm^{-1} on a Thermo Electron Corporation model Nexus 670 spectrophotometer equipped with FT-Raman module accessory. The ^1H and ^{13}C NMR spectra are taken in chloroform solutions and all signals are referenced to TMS on a BRUKER DPX-400 FT-NMR Spectrometer. All NMR spectra are recorded at room temperature.

COMPUTATIONAL DETAILS

The quantum chemical computations of 4-FPI were performed using the Gaussian 03 program package [10] at the DFT level using B3LYP (Becke's three parameter hybrid functional using Lee-Yang-Parr correlation functional) with 6-311G(d, p), 6-311++G(d, p) and cc-VPQZ basis sets. The vibrational modes were also assigned on the basis of TED analysis using SQM program [11]. The current version of the SQM package uses a modified procedure involving the scaling of individual valence coordinates (not the linear combinations present in natural internal coordinates). This has immediate advantages in terms of ease of use, as no natural internals need be generated (which may fail for

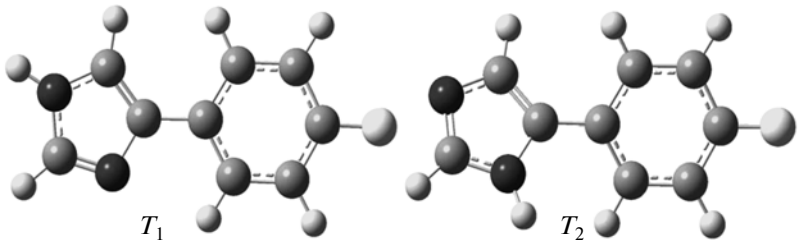

Fig. 1. Tautomeric forms of 4-FPI.

complicated molecular topologies) and it simplifies the classification and presorting of the coordinates. In addition, the extra flexibility involved in the scaling of individual primitive internals generally leads to an increase in accuracy and to more transferable scale factors [12]. The calculated vibrational wavenumbers are scaled by (0.967), (0.978) and (0.969), for B3LYP/6-311G(d, p), 6-311++G(d, p) and cc-pVQZ, respectively [13–15] to offset the systematic error caused by neglecting anharmonicity and electron density.

The GIAO (Gauge Including Atomic Orbital) method is one of the most common approaches for calculating isotropic nuclear magnetic shielding tensors [16, 17]. For the same basis set size GIAO method is often more accurate than those calculated with other approaches [18, 19]. The ^{1}H and ^{13}C NMR chemical shifts calculations of the T1 tautomeric form of the 4-FPI molecule were made by using B3LYP functional with 6-31G(d) basis set.

Predictions of Raman Intensities

The calculated Raman activities (S_i) was converted to relative Raman intensities (I_i) using the following relationship derived from the intensity theory of Raman scattering [20, 21]

$$I_i = \frac{f\left(\nu_0 - \nu_i\right)^4 S_i}{\nu_i\left[1 - \exp(-hc\nu_i/kT)\right]}, \qquad (1)$$

where, ν_0 is the exciting wavenumber, ν_i the vibrational wavenumber of the ith normal mode, h, c and k are fundamental constants, and f is a suitably chosen common normalization factor for all peak intensities. For simulation, the calculated FT-Raman spectra were plotted using pure Lorentzian band shape with a bandwidth of Full Width and Half Maximum (FWHM) of 10 cm^{-1}.

RESULTS AND DISCUSSION

Tautomeric Analysis

All the possible tautomeric forms of 4-FPI were calculated which are optimized by B3LYP/6-311G(d, p) level of theory. The possible two stable tautomeric forms are given in Fig. 1 which shows the possibility of proton transfer between the nitrogen atoms of imidazole ring. The total energies and the relative energies of the different tautomeric forms of 4-FPI are presented in Table 1. It is clear that the T_1 tautomer has the lowest energy and is the most stable form. The energy difference between T_1 and T_2 tautomer is 6.409 kJ/mol (at B3LYP/6-311G(d, p) level of theory). This confirms that the 4-FPI is the only stable tautomer in gas phase. The fluorine atom is connected to para position in 4-phenylimidazole and 4-FPI have similar tautomeric forms. The tautomeric equilibrium structures of 4-phenylimidazole molecule were investigated by several authors and is determined that T_1 is more stable than T_2 by 3 kJ/mol for AM1 and PM3 calculations by Ögretir et al. [22]. Maye and Venanzi calculated rotational barrier and energies of both T_1 and T_2 tautomeric forms of 4-PI [23]. They reported that the difference in energy is 7.5 kM/mol by T_1 compared with T_2. In the earlier work it shows that T_1 is more stable than T_2 by 5.27 kJ/mol by B3LYP/6-311G(d, p) level of theory. Due to the most stable state of T_1 tautomeric compared to T_2. So, finally T_1 tautomeric form was

Table 1. Total (a.u.) and relative energies (kcal/mol) and dipole moment (Debye) of different tautomers of 4-FPI calculated at the B3LYP levels of theory

Tautomer	Methods	Optimized ZPE corrected energy	Relative energy	E_{HOMO}, eV	E_{LUMO}, eV	$\Delta E_{HOMO-LUMO}$, eV	Dipole moment
T_1	B3LYP/6-311G(d, p)	−556.51303127	0.000	−5.807	−0.622	5.185	5.1913
	B3LYP/6-311++G(d, p)	−556.52477635	0.000	−5.968	−0.892	5.076	5.361
T_2	B3LYP/6-311G(d, p)	−556.51006100	7.798	−5.979	−0.969	5.010	2.7817
	B3LYP/6-311++G(d, p)	−556.52211306	6.992	−6.142	−1.205	4.937	2.7804

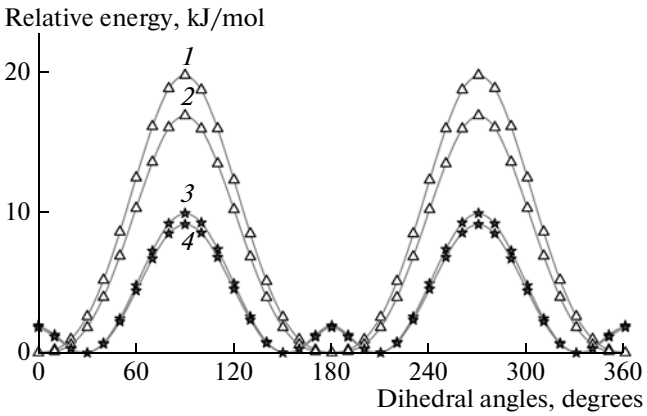

Fig. 2. Potential energy surface of tautomeric forms for dihedral angle N_{13}–C_{11}–C_3–C_2: T_1 (*1*, *2*), T_2 (*3*, *4*); B3LYP/6-311G(d, p) (*1*, *3*), BdLYP/6-311++G(d, p) (*2*, *4*).

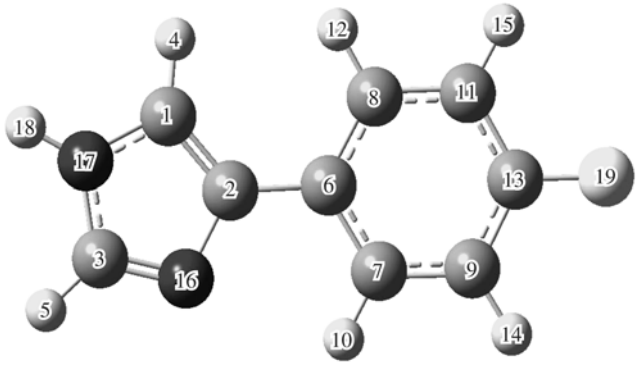

Fig. 3. Molecular structure of 4-FPI.

used in the future calculations such as vibrational and NMR spectra and NBO analysis of the 4-FPI molecule.

Conformational Analysis

In order to reveal all possible conformations of 4-FPI, a detailed potential energy surface (PES) scan in N_{16}–C_2–C_6–C_7 dihedral angles was performed. The scan was carried out by minimizing the potential energy in all geometrical parameters by changing the torsion angle for every 10° for a 360° rotation around the bond. The shape of the potential energy as a function of the dihedral angle is illustrated in Fig. 2. It shows that T_1 tautomeric form was planar (N–C–C–C dihedral angle for 0°) and T_2 tautomeric form was twisted (N–C–C–C dihedral angle for 35.3°) [23]. The T_1 tautomeric form predict a near planar equilibrium structure and the dihedral angle between phenyl and imidazole ring is 9° for HF/6-31G(d) level of theory [24]. In the 4-phenylimidazole molecule, predicted at 26.45° T_2 tautomeric form and 0° T_1 tautomeric form by B3LYP/6-311G(d, p) level of theory [9]. In this study the T_1 tautomeric shows the planar conformation (0°) and the T_2 tautomeric was twisted around (28.47°) at the B3LYP/6-311G(d, p) level of theory. The 4-phenylimidazole [9] and 4-FPI molecules exhibit similar trends for conformational analysis.

Optimized Geometry

The optimized molecular structure of the isolated 4-FPI molecule calculated using DFT at B3LYP/6-311++G(d, p) basis set is shown in Fig. 3. The computed optimized geometrical parameters along with the experimental values [25, 26] for comparison are given in Table 2. The predicted bond lengths of C_{11}–H_{15}, C_8–H_{12}, C_1–H_4, C_3–H_5 and C_9–H_{14} are elongated from the experimental values. The calculated dihedral angles C_8–C_6–C_2–N_{16} and C_8–C_6–C_2–C_1 are different at ~36.13° and ~39.92°, respectively, from the experimental values. Nielsen et al. [25] reported that T_1 conformer of title compound show in the crystalline states. According to X-ray data, dihedral angles between phenyl and imidazole group determine at about 30°. We investigated the most stable conformers of title compound for gas phase by using the theoretical methods. According to above discussions, T_1 conformer is the most stable conformer of title compound as shown in Table 1. T_1 conformer has planar geometry. Therefore, dihedral angles between phenyl and imidazole group determine at about 0 degrees as shown in Table 2. In 4-FPI calculated bond angles are H_{12}–C_8–C_{11} (120.1°) and C_2–C_1–H_4 (132.7°) and the corresponding experimental values are 119.08° and 129.19°, respectively. The differences in bond angles between experimental and calculated values may be due to the absence of steric repulsion between H_8 and H_{17} atoms. This is further supported by the bond distance between H_8 and H_{17} is 2.4181 Å.

From the geometry, the C_2–C_1 and C_{11}–C_{13} bond lengths of 4-phenylimidazole were calculated as 1.393 and 1.394 Å by using B3LYP/6-31G(d, p) level [9]. These bond lengths of 4-FPI are predicted at 1.386 Å at the same basis set. The other C–C bond lengths of Phenyl group have not changed due to fluorine coordination which shows that C_2–C_1 and C_{11}–C_{13} bond lengths are sensitive to fluorine substitution.

In the Imidazole ring, the calculated bond lengths of C_1–N_{17}, C_2–N_{16}, and C_3–N_{16} are 1.3834, 1.3772, and 1.3092 Å, respectively. It clearly shows the hyperconjugation between lone pair electrons of N_{16} atom with neighboring atoms.

Mulliken Charge Distribution Analysis

The Mulliken atomic charges were calculated at the B3LYP/6-311G(d, p) basis set. Figure 4 shows the Mulliken atomic net charges in 4-FPI. The atoms N_{17} and N_{16} shows more negative (–0.3337e) and

Table 2. Optimized parameters of T_1 tautomeric form of 4-FPI for B3LYP calculation

Bond length, Å	B3LYP 6-311G(d,p)	B3LYP 6-311/++ G(d,p)	B3LYP cc-pVQZ	XRD
C_{11}–C_8	1.390	1.391	1.387	1.391
C_8–C_6	1.402	1.402	1.398	1.400
C_6–C_7	1.402	1.402	1.398	1.398
C_7–C_9	1.390	1.391	1.387	1.392
C_9–C_{13}	1.385	1.385	1.382	1.388
C_{11}–C_{15}	1.083	1.082	1.080	0.979
C_8–C_{12}	1.084	1.084	1.081	0.954
C_6–C_2	1.468	1.469	1.466	1.473
C_7–H_{10}	1.082	1.082	1.079	0.981
C_9–H_{14}	1.083	1.083	1.080	0.986
C_{13}–F_{19}	1.353	1.358	1.351	1.359
C_{13}–C_{11}	1.386	1.386	1.383	1.390
C_2–C_1	1.378	1.378	1.375	1.373
C_1–N_{17}	1.377	1.378	1.373	1.375
N_{17}–C_3	1.364	1.365	1.360	1.351
C_3–N_{16}	1.309	1.309	1.306	1.326
N_{16}–C_2	1.383	1.383	1.380	1.389
C_1–H_4	1.076	1.076	1.073	0.966
N_{17}–H_{18}	1.007	1.007	1.004	0.851
C_3–H_5	1.079	1.079	1.076	0.970
Bond Angle, deg				
C_{11}–C_8–C_6	121.2	121.2	121.2	120.3
C_8–C_6–C_7	118.2	118.3	118.2	119.1
C_6–C_7–C_9	121.0	121.0	121.1	120.2
C_7–C_9–C_{13}	118.0	118.7	118.8	120.3
C_9–C_{13}–C_{11}	121.7	122.0	121.8	119.8
C_9–C_{13}–F_{19}	119.2	119.0	119.1	119.3
C_{11}–C_{13}–F_{19}	119.0	118.8	118.9	118.4
H_{12}–C_8–C_{11}	120.1	120.1	118.6	119.0
H_{10}–C_7–C_6	118.4	118.7	118.6	120.3
C_{13}–C_{11}–H_{15}	119.5	119.8	119.8	120.2
C_{13}–C_9–H_{14}	119.5	119.8	119.7	121.5
C_8–C_6–C_2	121.9	121.7	121.7	119.9
C_7–C_6–C_2	119.7	119.9	120.0	120.9
C_6–C_2–C_1	129.3	129.	129.2	127.8
C_2–C_1–H_4	132.7	132.6	132.6	129.1
C_2–N_{16}–C_3	106.1	106.2	106.2	105.3
C_2–C_1–N_{17}	105.6	105.6	105.7	106.1
C_1–N_{17}–H_{18}	126.0	126.1	126.1	126.5
H_{18}–N_{17}–C_3	126.6	126.6	126.5	125.6
N_{17}–C_3–H_5	122.5	122.5	122.5	123.5
Dihedral Angle, deg				
C_{11}–C_8–C_6–C_7	−0.000	−0.000	−0.000	−1.09
C_8–C_6–C_7–C_9	0.000	0.001	0.001	1.36

Table 2. (Contd.)

Dihedral Angle, deg	B3LYP 6-311G(d,p)	B3LYP 6-311/++ G(d,p)	B3LYP cc-pVQZ	XRD
$C_6–C_7–C_9–C_{13}$	0.000	0.000	0.000	−0.68
$H_{15}–C_{11}–C_{13}–F_{19}$	0.000	0.000	0.000	1.06
$H_{14}–C_9–C_{13}–F_{19}$	0.000	0.000	0.000	−1.32
$F_{19}–C_{13}–C_{11}–C_8$	180.0	180.0	−179.9	−178.9
$F_{19}–C_{13}–C_9–C_7$	180.0	179.9	180.0	178.6
$H_{12}–C_8–C_6–C_2$	−0.001	−0.000	−0.002	−2.48
$H_{10}–C_7–C_6–C_2$	0.000	0.000	0.001	1.75
$C_8–C_6–C_2–C_1$	−0.010	−0.005	−0.019	−39.92
$C_7–C_6–C_2–N_{16}$	−0.007	−0.010	−0.020	−38.6
$C_6–C_2–C_1–N_{17}$	−179.9	−179.9	180.0	−176.5
$C_6–C_2–N_{16}–C_3$	179.9	179.9	180.0	176.7
$C_6–C_2–C_1–H_4$	0.000	0.002	0.002	6.12
$H_4–C_1–N_{17}–H_{18}$	−0.007	−0.005	−0.013	−10.11
$H_{18}–N_{17}–C_3–H_5$	0.004	0.016	0.019	4.64
$N_{17}–C_3–N_{16}–C_2$	0.018	0.056	0.027	0.06
$C_2–C_1–N_{17}–H_{18}$	179.9	179.9	179.9	172.3
$C_2–N_{16}–C_3–H_5$	−179.9	−179.9	180.0	−177.8
$C_7–C_6–C_2–C_1$	179.9	179.9	179.9	137.5
$C_8–C_6–C_2–N_{16}$	179.9	179.9	179.9	143.8

(–0.3325e) charge respectively and C_3 atoms have more positive charge (0.1692e), which suggests extensive charge derealization in the molecule. Nature of C atom have negative charge but in 4-FPI except C_{13}, C_2, C_1, and C_3 are having positive (0.2435, 0.02465, 0.0657 and 0.1692e) charge, showing that these are bonded with heavy electro negative atoms (C–F, C–N). The shortening of the C_3=N_{16} bond (Table 1) also supports this conclusion. Normally hydrogen atoms have positive charge, but in 4-FPI H_{18} having more positive charge (0.2292e) in comparison with other hydrogen atoms, it shows that the electron pass through into the nitrogen atom to the imidazole ring. Similarly, more positive charge (0.2435e) observed in C_{13} atom bonded to the fluorine atom shows charge transfer from the fluorine atom to phenyl ring.

NBO ANALYSIS

The natural bonding orbital (NBO) calculations were performed using the NBO 3.1 program [27] as implemented at the B3LYP/6-31G(d) level basis set. The larger the $E(2)$ value, the more intensive is the interaction between electron donors and electron acceptors, i.e., the more donating tendency from electron donors to electron acceptors and the greater the extent of conjugation of the whole system. Derealization of electron density between occupied Lewis-type (bond or lone pair) NBO orbitals and formally unoccupied (antibond or Rydgberg) non-Lewis NBO orbitals correspond to a stabilizing donor–acceptor interaction. The intramolecular interaction are formed by the orbital overlap between π(C–C) and π*(C–C) antibond orbital which results intramolecular charge transfer (ICT) causing stabilization of the system. These interactions are observed as increase in electron density (E_D) in C–C antibonding orbital that

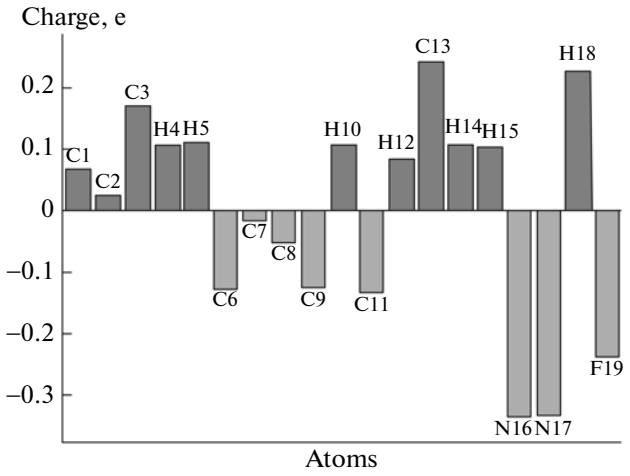

Fig. 4. Mulliken charge distributions diagram.

Table 3. Second order perturbation theory analysis of Fock matrix in NBO basis

Donor (*i*)	E_D (*i*), e	Acceptor (*j*)	E_D (*j*), e	$E(2)$[a], kJ mol^{-1}	$E(j)-E(i)$[b], arb. un.	$F(i,j)$[c] arb. un.
$\pi(C_{11}-C_8)$	1.6988	$\pi^*(C_6-C_7)$	0.3707	17.94	0.30	0.066
		$\pi^*(C_9-C_{13})$	0.3790	22.07	0.28	0.072
$\pi(C_6-C_7)$	1.6249	$\pi^*(C_9-C_{13})$	0.3790	20.88	0.27	0.067
		$\pi^*(C_{11}-C_8)$	0.3413	22.45	0.27	0.070
		$\pi^*(C_2-C_1)$	0.3373	19.05	0.27	0.064
$\pi(C_9-C_{13})$	1.6575	$\pi^*(C_{11}-C_8)$	0.3413	19.45	0.29	0.067
		$\pi^*(C_6-C_7)$	0.3707	20.61	0.30	0.071
$\pi(C_2-C_1)$	1.8121	$\pi^*(C_3-N_{16})$	0.3661	15.13	0.27	0.060
		$\pi^*(C_6-C_7)$	0.3707	12.26	0.31	0.058
$\pi(C_3-N_{16})$	1.8746	$\pi^*(C_2-C_1)$	0.3373	21.27	0.34	0.080
$n_1(N_{17})$	1.5819	$\pi^*(C_3-N_{16})$	0.3661	46.14	0.29	0.104
$n_1(N_{17})$	1.5819	$\pi^*(C_2-C_1)$	0.3373	30.36	0.31	0.088
$n_1(N_{16})$	1.9201	$\sigma^*(N_{17}-C_3)$	0.0345	7.89	0.81	0.072
$n_3(F_{19})$	1.9247	$\pi^*(C_9-C_{13})$	0.3790	18.38	0.43	0.086
$\pi^*(C_{11}-C_8)$	0.3413	$\pi^*(C_6-C_7)$	0.3707	253.19	0.01	0.082
$\pi^*(C_9-C_{13})$	0.3790	$\pi^*(C_6-C_7)$	0.3707	208.31	0.02	0.082
$\pi^*(C_2-C_1)$	0.3373	$\pi^*(C_6-C_7)$	0.3707	137.41	0.01	0.067
$\pi^*(C_3-N_{16})$	0.3661	$\pi^*(C_2-C_1)$	0.3373	74.85	0.02	0.061
$\sigma(C_1-N_{17})$	1.9855	$\sigma^*(C_6-C_2)$	0.0338	4.62	1.31	0.070
$\sigma(C_7-C_9)$	1.9730	$\sigma^*(C_{13}-F_{19})$	0.0330	4.11	0.97	0.056
		$\sigma^*(C_6-C_2)$	0.0338	3.46	1.19	0.057
$\sigma(C_{11}-C_8)$	1.9729	$\sigma^*(C_{13}-F_{19})$	0.0330	4.02	0.97	0.056

[a] $E(2)$ means energy of hyper conjugative interactions.
[b] Energy difference between donor and acceptor *i* and *j* NBO orbitals.
[c] $F(i,j)$ is the Fock matrix element between *i* and *j* NBO orbital.

weakens the respective bonds. The most important interactions between filled (donors) Lewis-type NBO and empty (acceptors) non-Lewis NBOs are reported in Table 3.

In Fluorophenyl ring the E_D at the two conjugated π bond (~1.6e) and π* bond (~0.3e) clearly demonstrate the strong derealization. But the Imidazole conjugated π bonds (~1.8e) and π* bonds (~0.3e) shows a lesser degree of conjugation.

A different level of π-electron derealizations is observed in the imidazole ring between (C_2-C_1) and (C_3-N_{16}), with 30 and 46 kcal/mol, respectively. This happens because the $n_1(N_{17})$ donate more electrons to $\pi^*(C_3-N_{16})$ than to $\pi^*(C_2-C_1)$, thereby enhancing the population at $\pi^*(C_3-N_{16})$ and N_{16} becomes more electronegative (–0.3325e charge). The enhanced $\pi^*(C_{11}-C_8)$ NBO further conjugates with $\pi^*(C_6-C_7)$, resulting in an enormous stabilization 253.19 kcal/mol. The atom N_{17} becomes more electronegative (–0.3337e), as the amount of charge transferred from $n_1(N_{17})$, orbitals is very low, which makes imidazole ring a highly chelating agent [28].

VIBRATIONAL ANALYSIS

The 4-FPI molecule consists of 19 atoms. So, there are 51 vibrational modes ranging from 32–3533 cm^{-1}. The 51 vibrational modes of 4-FPI have been assigned according to the detailed motion of the individual atoms. This molecule belongs to C_1 symmetry group. The experimental FT-IR and FT-Raman along with the calculated wavenumbers are given in Table 4. As seen in tables, IR and Raman intensities of 4-FPI are in consistency with the TED results. The theoretically predicted IR and Raman spectra at B3LYP/6-311++G(d, p) level of calculations along with experimental FT-IR and FT-Raman spectra are shown in Figs. 5, 6.

Fluorophenyl Ring Vibrations

Fluorine (heavy electro negative) atom and imidazole rings are substituted in para position with the phenyl ring. The detailed analysis of vibrational wavenumbers for various functional groups of Fluorophenyl ring are discussed below.

Table 4. Vibrational assignment of 4-FPI by TED analysis based on SQM force field calculations

Mode No.	Assignment	4-(4-Fluoro-phenyl)-1H-imidazole					4-Phenylimidazole		TED, %
		Theoretical, cm^{-1}			Experimental, cm^{-1}		Experimental, cm^{-1}		
		a	b	c	IR	Raman	IR	Raman	
υ_1	Ring Torsion	32	32	27					$\Gamma_{CCCN}(95)$ P-IM
υ_2	Ring Torsion	81	82	81				62	$\Gamma_{CCCC}(58)$ P + $\gamma_{CNCC}(24)$ IMI
υ_3	CCC Bend P-IMI	137	139	138					$\delta_{CCC}(44)$ P + $\delta_{CCC}(28)$ + $\gamma_{CNCC}(16)$ I
υ_4	Ring Torsion	214	217	215				143	$\gamma_{CNCC}(28)$ I + $\Gamma_{CCCC}(22)$ + $\delta_{CCC}(14)$ + $\gamma_{FCCC}(13)$ P
υ_5	CC Str P-IMI	307	311	308				307	$\upsilon_{CC}(31)$ P-IM + $\delta_{CCC}(21)$ P + $\delta_{CCN}(11)$ + IM
υ_6	FCC bend	365	369	368				346	$\delta_{FCC}(38)$ + $\delta_{CCC}(11)$ P
υ_7	Ring Torsion	372	377	373				404	$\Gamma_{CCCC}(20)$ + $\gamma_{FCCC}(25)$ + $\delta_{FCC}(13)$ P
υ_8	Ring Bend	409	414	412	419	419	433	431	$\Gamma_{HCCC}(93)$ P
υ_9	FCC Bend CCC Bend (P-IMI)	458	463	460	461	461			$\delta_{FCC}(24)$ + $\delta_{CCC}(21)$ P + $\delta_{CCC}(14)$ P-IM
υ_{10}	Ring Torsion	505	511	509					$\Gamma_{HNCN}(36)$ IM + $\gamma_{FCCC}(15)$ P
υ_{11}	Ring Torsion	513	519	513	529		521	521	$\Gamma_{HNCN}(46)$ IM + $\gamma_{FCCC}(11)$ P
υ_{12}	CCC Bend	594	601	597	602	600	598	618	$\delta_{CCC}(32)$ + $\upsilon_{FC}(15)$ P + $\upsilon_{CC}(15)$ P-IM + $\delta_{CCN}(10)$ IM
υ_{13}	CCC Bend	628	636	630	624	633	632	631	$\delta_{CCC}(69)$ P
υ_{14}	Ring Bend	631	638	632					$\Gamma_{NCNC}(54)$ + $\Gamma_{HNCN}(13)$ + $\Gamma_{CCNC}(13)$ + IM
υ_{15}	Ring Bend	678	686	683					$\Gamma_{CCNC}(46)$ + $\Gamma_{HCNC}(12)$ + $\Gamma_{NCNC}(12)$ IM
υ_{16}	Ring Bend	696	704	709	693	695	699	681	$\Gamma_{CCCC}(77)$ P
υ_{17}	Oop CCH Bend	743	752	752	775	778	760	760	$\Gamma_{HCNC}(83)$ + $\Gamma_{NCNC}(16)$ IM
υ_{18}	Oop CCH Bend	795	804	802			787	787	$\Gamma_{HCCC}(92)$ P
υ_{19}	CC FC Stretching	799	808	807	809	812			$\upsilon_{CC}(45)$ + $\upsilon_{FC}(23)$ P
υ_{20}	Oop CCH Bend	804	813	808					$\Gamma_{HCNC}(41)$ IM + $\Gamma_{HCCC}(26)$ P
υ_{21}	Oop CCH Bend	833	842	841	832	841	842	849	$\Gamma_{HCNC}(41)$ IM
υ_{22}	Ip CNC Bend	911	922	913	889	926	895		$\delta_{CNC}(66)$ IM
υ_{23}	Oop CCH Bend	913	924	924			919		$\Gamma_{HCCC}(78)$ P
υ_{24}	Oop CCH Bend	922	932	931					$\Gamma_{HCCC}(72)$ P
υ_{25}	Ip CNC Bend	957	968	965	955	955	958	957	$\delta_{NCN}(41)$ + $\delta_{CCN}(10)$ IM
υ_{26}	Ip CCC Bend	996	1008	1002	1015	1013	1009	1000	$\delta_{CCC}(74)$ + $\delta_{HCC}(13)$ P
υ_{27}	NCH CCH Bend	1041	1053	1044	1060	1061	1062		$\delta_{NCN}(22)$ + $\delta_{HNC}(14)$ + $\delta_{HCN}(12)$ IM
υ_{28}	NC Str, NCH Bend	1074	1086	1076					$\upsilon_{NC}(44)$ + $\delta_{HNC}(24)$ + $\delta_{HCN}(13)$ IM
υ_{29}	Ip CCH Bend	1084	1096	1088	1094	1094			$\delta_{HCC}(62)$ + $\upsilon_{CC}(24)$ P
υ_{30}	NC Stretching	1095	1107	1098	1113	1111	1109	1113	$\upsilon_{NC}(55)$ + $\delta_{HCN}(16)$ IM
υ_{31}	Ip CCH Bend	1138	1151	1144	1159	1158	1157	1154	$\delta_{HCC}(65)$ P
υ_{32}	NCH, CCH Bend	1194	1208	1201	1217	1216	1226	1225	$\delta_{HCN}(50)$ + $\upsilon_{CC}(11)$ IM
υ_{33}	FC Stretching	1213	1227	1211	1241		1261	1258	$\upsilon_{FC}(46) - \upsilon_{CC}(22)$ + $\delta_{HCC}(21)$ P
υ_{34}	NC Stretching	1256	1270	1258	1277	1277	1284	1281	$\upsilon_{NC}(28)$ + $\delta_{HCN}(14)$ IM
υ_{35}	CC (P-IMI)	1278	1292	1282		1293			$\upsilon_{CC}(26)$ + $\delta_{HCN}(16)$ IM
υ_{36}	Ip CCH Bend	1290	1305	1295					$\delta_{HCC}(72) - \upsilon_{CC}(10)$ P
υ_{37}	NC Stretching	1311	1327	1314	1313	1312	1309	1310	$\upsilon_{NC}(22)$ + $\delta_{CCN}(21)$ IM

Table 4. (Contd.)

Mode No.	Assignment	4-(4-Fluoro-phenyl)-1H-imidazole					4-Phenylimidazole		TED, %
		Theoretical, cm^{-1}			Experimental, cm^{-1}		Experimental, cm^{-1}		
		a	b	c	IR	Raman	IR	Raman	
υ_{38}	NCH Bend	1395	1411	1400	1406	1403			$\delta_{HNC}(31) + \upsilon_{CC}(11) + \upsilon_{NC}(19)$ IM
υ_{39}	CC Stretching	1408	1424	1407					$\upsilon_{CC}(27)$ P
υ_{40}	NC Str + NCH Bend	1470	1487	1474	1459	1464	1422	1441	$\upsilon_{NC}(34) + \delta_{HCN}(23) + \upsilon_{CC}(17)$ IM
υ_{41}	Ip CCH Bend	1490	1507	1494	1491	1489	1465	1466	$\delta_{HCC}(49)$ P
υ_{42}	CC Stretching	1537	1555	1539		1513			$\upsilon_{CC}(25)$ IM + $\upsilon_{CC}(15)$ P-IM
υ_{43}	CC Stretching	1577	1595	1580	1563	1563	1579	1580	$\upsilon_{CC}(48)$ P
υ_{44}	CC Stretching	1599	1617	1598	1608	1609	1606	1607	$\upsilon_{CC}(29)$ P
υ_{45}	CH Stretching	3068	3103	3076					$\upsilon_{CH}(93)$ P
υ_{46}	CH Stretching	3087	3122	3093					$\upsilon_{CH}(99)$ P
υ_{47}	CH Stretching	3093	3128	3099	3004	3005	2992	2992	$\upsilon_{CH}(90)$ P
υ_{48}	CH Stretching	3103	3138	3108	3056	3071	3052	3061	$\upsilon_{CH}(96)$ P
υ_{49}	CH Stretching	3135	3171	3142					$\upsilon_{CH}(99)$ IM
υ_{50}	CH Stretching	3163	3199	3170					$\upsilon_{CH}(99)$ IM
υ_{51}	NH Stretching	3533	3573	3538	3100	3119	3119	3119	$\upsilon_{NH}(100)$ IM

[a] 6311G(d, p) with scaling factor 0.967.
[b] 6311++G(d, p) with scaling factor 0.978.
[c] cc-pVQZ with scaling factor 0.969.

C–H vibrations. Normally the aromatic ring C–H stretching vibrations are observed in the IR region at 3080–3010 cm^{-1} [29]. Güllüoğlu et al. [9] assigned the C–H stretching in FT-IR and FT-Raman data at 3052, 2992 cm^{-1} and 3061, 2922 cm^{-1}, respectively. Similarly, in the fluorophenyl ring C–H stretching vibration was observed at 3004–3056 cm^{-1} in FT-IR and 3005, 3070 cm^{-1} at FT-Raman, respectively, at

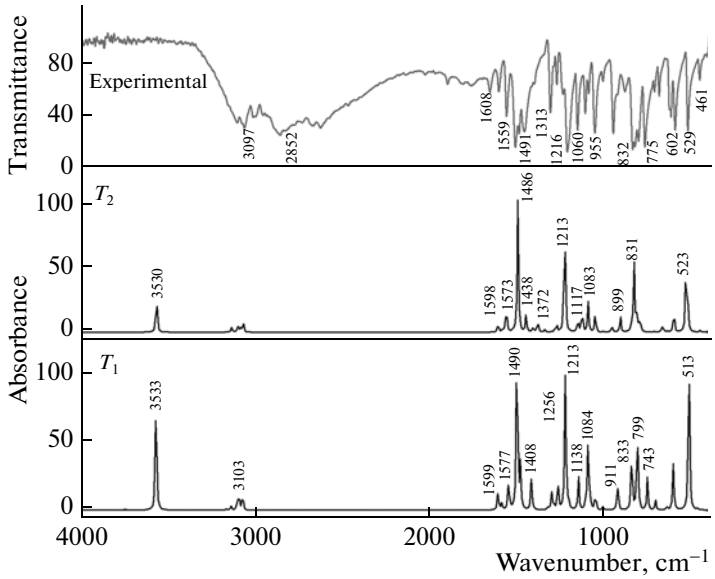

Fig. 5. The FT-IR spectra of 4-FPI in the range 4000–250 cm^{-1}.

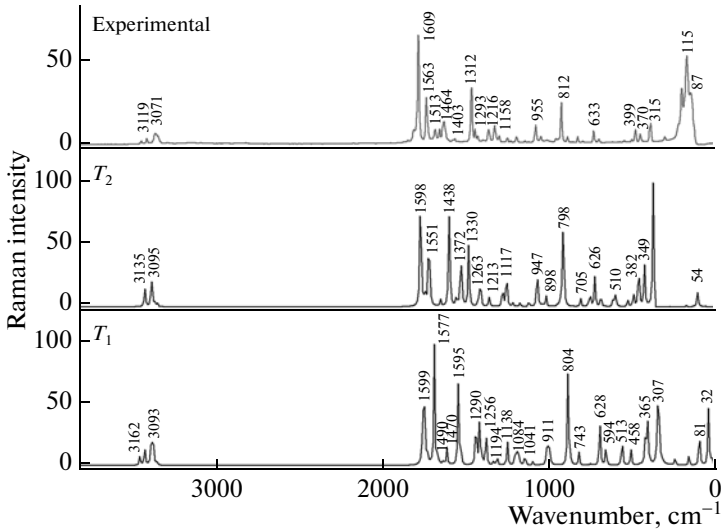

Fig. 6. The FT-Raman spectra of 4-FPI in the range 4000–0 cm^{-1}.

the same mode. The TED corresponding to this vibrations is a pure mode with contributions of 96%. All the aromatic C–H stretching bands are found to be weak and this is due to decrease of dipole moment caused by reduction of the negative charge on the carbon atom. This reduction occurs because of the electron withdrawal on the carbon atom by the substituent due to the decrease of inductive effect, which in turn caused by the increase in chain length of the substituent [30].

Normally the C–H in-plane deformation bands occur in the region 1300–1000 cm^{-1} at FT-IR [31]. Additional difficulties may also arise due to the presence of other bands in the region. C–H in-plane bending of Fluorophenyl ring is observed in FT-IR at 1159 and at 1094 cm^{-1} (Mode nos. 29, 31) and also same region in FT-Raman. The C–C–H in-plane deformation wavenumbers are observed in 1491 and 1489 cm^{-1} (Mode no. 41) in FT-IR and in FT-Raman, respectively. The TED corresponding to this vibration is a pure mode with contributions of 49% and also medium peaks observed in FT-IR spectrum.

C–C vibrations. Aromatic C=C stretching vibrations occur in the region 1625–1430 cm^{-1} in FT-IR [29]. Fluorophenyl ring C–C stretching bands are observed at 1608 and 1563 cm^{-1} in FT-IR. The other C–C stretching vibrations are observed in FT-IR and FT-Raman at 809 and 812 cm^{-1}. C–C bending vibrarions for para-disubstituted benzenes with electron-donating substituents occurs at 520–490 cm^{-1} [29]. Fluorophenyl ring bending mode is observed in FT-IR at 693 cm^{-1} and FT-Raman at 695 cm^{-1}, 77% (TED).

C–F vibrations. The C–F stretching vibrations generally occur in the region 1360–1000 cm^{-1} [29, 32]. Observation of bands at 1241 cm^{-1} in FT-IR has been assigned to C–F stretching vibrations.

Imidazole Ring Vibrations

Imidazole have several bands of variable intensity in the range 1660–1450 cm^{-1} in FT-IR due to C=N and C=C stretching vibrations [29].

C–H vibrations. Imidazole C–H vibrations are distinctly observed in FT-Raman at 3145, 3115 cm^{-1} as strong bands and at 3115, 3100 cm^{-1} FT-IR as weak bands as expected [33]. Theoretically predicted wavenumbers at 3135 and 3163 cm^{-1} are assigned to C–H stretching vibrations. The TED corresponds to this vibration is a pure mode with contribution of 99%, but the recorded spectra fails to show peaks for the corresponding bands in the above said region.

C–N vibrations. According to Güllüoğlu et al. [9] the –N stretching appears at 1395 cm^{-1} for 4-phenylimidazole. The series of bands observed in FT-IR at 1459, 1406, 1313, 1277 and 1113 cm^{-1} and in FT-Raman at 1464, 1403, 1312, 1277 and 1111 cm^{-1} make significant contributions to N–C stretching mode. The C–N–C in-plane deformation vibrations are observed at 889, 955 cm^{-1} in FT-Raman and at 926, 955 cm^{-1} in FT-IR spectrum.

C–C vibrations. In the imidazole ring C–C stretching is observed in FT-Raman at 1513, 1293 cm^{-1} (Mode nos. 35, 42) and absent in FT-IR, corresponding to this vibration is a pure mode contribution of 25% (TED), weak peak are observed in FT-Raman but absent in FT-IR.

N–H vibrations. The heteroaromatic molecule containing an N–H group occurs in the region 3500–3220 cm^{-1}. The position of absorption in this region depends upon the degree of hydrogen bonding, and hence upon the physical state of the sample or the polarity of the solvent [34]. In the 4-phenylimidazole, N–H vibrations are observed at 3119 cm^{-1} in FT-IR

Table 5. Experimental and theoretical chemical shifts (^{13}C, ^{1}H) of 4-FPI by B3LYP/6-31G(d) method, δ(ppm)

Atom	Experimental	B3LYP/6-31G(d)
C_{13}	163.24	153.74
C_3	135.56	125.47
C_2	135.56	132.44
C_{11}	115.75	108.61
C_9	115.75	108.94
C_8	126.64	117.77
C_7	126.64	119.82
H_{18}	8.93	8.39
H_{12}	7.7	7.43
H_{10}	7.7	8.13
H_{14}	7.3	6.82
H_{15}	7.3	6.77
H_5	7.7	7.24
H_4	7.1	7.07

spectrum [9]. For the 4-FPI compound, the N–H stretching vibration is observed in the same region 3100 and 3119 cm^{-1} (Mode no. 51) at FT-IR and FT-Raman, respectively.

NMR ANALYSIS

The isotropic chemical shifts are frequently used as an aid in identification of reactive ionic species. It is recognized that accurate predictions of molecular geometries are essential for reliable calculations of magnetic properties. The NMR spectra calculations were performed for chloroform ($CDCl_3$) and in dimethylsulfoxide (DMSO) solvent. It is necessary to consider the solvent effects because the spectral data available are obtained in different solutions. The isotropic shielding values were used to calculate the isotropic chemical shifts d with respect to tetramethylsilane (TMS) $\sigma_{iso}^{X} = \sigma_{iso}^{TMS} - \sigma_{iso}^{X}$. The values of $\sigma_{iso}^{TMS}S$ are 182.46 and 31.88 ppm for ^{1}C and ^{13}H NMR spectra, respectively [35, 36].

Application of the GIAO [16] approach to molecular systems was significantly improved by an efficient application of the method to the ab initio SCF calculations, using techniques borrowed from analytic derivative methodologies. GIAO procedure is somewhat superior since it exhibits a faster convergence of the calculated properties upon extension of the basis set used. Taking into account the computational cost and effectiveness of calculations, the GIAO method seems to be preferable from many aspects at the present state of this subject, on the other bands, the density functional methodologies offer an effective alternative to the conventional correlated methods, due to their significantly lower computational cost [37]. The ^{1}H and ^{13}C chemical shifts were measured in a less polar ($CDCl_3$) solvent. The range of the ^{13}C NMR chemical shifts for a typical organic molecule usually is >100 ppm [35, 36].

The full geometry optimization of 4-FPI was performed by using B3LYP/6-311G(d) method. Then Gauge-including atomic orbital (GIAO) ^{1}H and ^{13}C chemical shift calculations of the compound have been made by the same method. Chemical shift values are shown in Table 5.

In the present study, the signals for carbons were observed at 115–163 ppm. The carbon atoms C_{13} and C_3 are highly electropositive atom, resulting at higher chemical shift (150.2 ppm) due to more positive charge. C_{11}, C_9, C_1 have less values comparing to the other carbon atoms. The NMR observation for H_{18} atom has been recorded, from that the theoretical value obtained at 8.39 ppm, it is nearly equal to the experimental value 8.93 ppm.

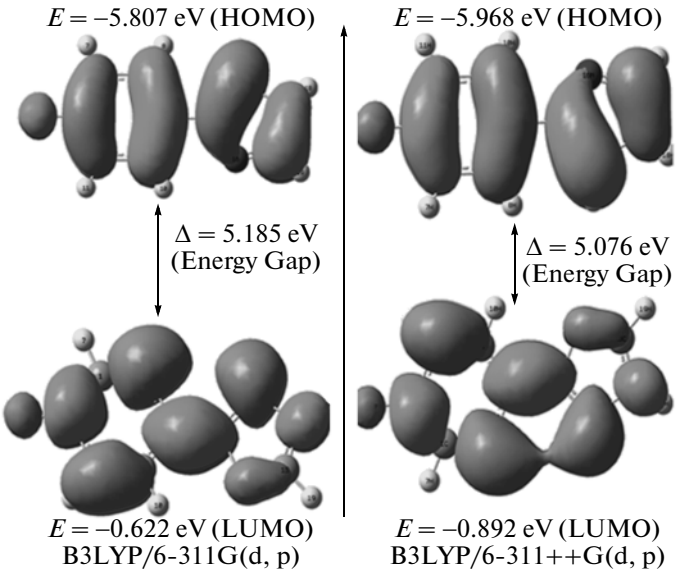

Fig. 7. HOMO-LUMO diagram of 4-FPI in two various basis sets.

HOMO-LUMO ANALYSIS

Many organic molecules containing conjugated π-electrons are characterized by their hyperpolarizabilies and were analyzed by means of vibrational spectroscopy [38, 39]. Owing to the interaction between HOMO and LUMO orbital of a structure, the transition state of π–π*-type is observed with regard to the molecular orbital theory [40]. The energies of the highest occupied molecular orbital (HOMO) and the lowest unoccupied molecular orbital (LUMO) are computed at the B3LYP/6-311G(d, p) and B3LYP/6-311++G(d, p) basis sets. HOMO and LUMO orbitals

are shown in Fig. 7. Generally, the energy values of LUMO and HOMO and their energy gap reflect the chemical activity of the molecule which is an important stability condition for the structure [41]. HOMO as an electron donor represents the ability to donate an electron, while LUMO as an electron acceptor represents the ability to obtain an electron. The smaller the LUMO-HOMO energy gap, the easier it is for the HOMO electrons to be excited. The HOMO, LUMO energy gap values are 5.185 and 5.076 eV by B3LYP/6-311++G(d, p) and B3LYP/6-311G(d, p) basis set, respectively. The calculated HOMO and LUMO energies clearly show that charge transfer occurs within the molecule.

CONCLUSIONS

The imidazole derivative plays a primary role in the functional architecture of biologically active molecules such as novel histamine H_2 receptor antagonists, cardiotropic agents and several types of artificial enzymes. Imidazole derivative have the important biological, pharmaceutical and chemical properties. A complete vibrational analysis of 4-FPI was performed using Density functional theory basis. The wavenumbers proposed by TED calculations are in fair agreement with the observed wavenumbers. T_1 tautomer has the lowest energy and is the most stable form compared to T_2 tautomer calculated at RB3LYP/6-311G(d, p) level basis set C–C bond lengths vary in the ring due to fluorine coordination. The enhanced $\pi^*(C_{11}–C_8)$ NBO further conjugates with $\pi^*(C_6–C_7)$, resulting in an enormous stabilization of energy. Comparing to other carbon atoms, C_{13} directly bonded with fluorine atom has more positive charge 0.2435e which shows electron transfer from the fluorine atom to the phenyl ring. HOMO-LUMO energy gap shows that T_1 (tautomer) is greater than that of T_2 (tautomer), this also gives an evidence for T_1 more stable than T_2. We hope that the results will be of help in the guess of the experimental and theoretical evidence for the title molecule in antibacterial, antifungal, antiprotozoal, and anthelmintic activity.

ACKNOWLEDGMENTS

The author (Y. Erdogdu) would like to thank Ahi Evran University Research Fund for its financial support. We would like to thank the central laboratory of METU (ODTÜ) for recording FT-Raman spectra, Gazi University Art and Science Faculty Department of Chemistry for recording FT-IR spectra.

REFERENCES

1. S. O. P. Kuzmonovic, L. M. Leovac, N. V. Perisicjanjic, J. Rogan, and J. Balaz, J. Serb. Chem. Soc. **64**, 381(1999).
2. L. S. Ahuja, and I. Prasad, Inorg. Nucl. Chem. Lett. **12**, 777 (1976).
3. Arturo Donetti, Enzo Cereda, Elio Bellora, Alberto Gallazzi, Cesare Bazzano, Piercarlo Vanoni, Piero Del Soldato, Rosamaria Micheletti, Ferdinando Pagani, and Antonio Giachetti, J. Med. Chem. **27**, 380 (1984).
4. P. W. Erhardt, A. A. Hagedorn, 3rd, and M. Sabio, Mol. Pharmacol. **33**, 1 (1988).
5. D. J. Cram, L. P. Yuk Sun, and Ho Siew Peng, J. Am. Chem. Soc. **108**, 839 (1986)
6. J. Cram Donald and Edan Katz Howard, J. Am. Chem. Soc. **105**, 135 (1983).
7. T. D'Souza, Valerian K. Hanabusa, T. O'Leary, C. Gadwood Robert, and Myron L. Bender, Biochem. Bioph. Res. Co. **129**, 727 (1985).
8. I. M. Mallick, V. T. D'Souza, M. Yamaguchi, J. Lee, P. Chalabi, R. C. Gadwood, and M. L. Bender, J. Am. Chem. Soc. **106**, 7252 (1984).
9. M. T. Güllüoğlu, Y. Erdogdu, J. Karpagam, N. Sundaraganesan, and Ş. Yurdakul, J. Mol. Struct. **990**, 14 (2011).
10. M. J. Frisch, G. W. Trucks, H. B. Schlegel, G. E. Scuseria, M. A. Robb, J. R. Cheeseman, J. A. Montgomery, Jr., T. Vreven, K. N. Kudin, J. C. Burant, J. M. Millam, S. S. Iyengar, J. Tomasi, V. Barone, B. Mennucci, M. Cossi, G. Scalmani, N. Rega, G. A. Petersson, H. Nakatsuji, M. Hada, M. Ehara, K. Toyota, R. Fukuda, J. Hasegawa, M. Ishida, T. Nakajima, Y. Honda, O. Kitao, H. Nakai, M. Klene, X. Li, J. E. Knox, H. P. Hratchian, J. B. Cross, C. Adamo, J. Jaramillo, R. Gomperts, R. E. Stratmann, O. Yazyev, A. J. Austin, R. Cammi, C. Pomelli, J. W. Ochterski, P. Y. Ayala, K. Morokuma, G. A. Voth, P. Salvador, J. J. Dannenberg, V. G. Zakrzewski, S. Dapprich, A. D. Daniels, M. C. Strain, O. Farkas, D. K. Malick, A. D. Rabuck, K. Raghavachari, J. B. Foresman, J. V. Ortiz, Q. Cui, A. G. Baboul, S. Clifford, J. Cioslowski, B. B. Stefanov, G. Liu, A. Liashenko, P. Piskorz, I. Komaromi, R. L. Martin, D. J. Fox, T. Keith, M. A. Al-Laham, C. Y. Peng, A. Nanayakkara, M. Challacombe, P. M. W. Gill, B. Johnson, W. Chen, M. W. Wong, C. Gonzalez, and J. A. Pople, Gaussian 03, Revision C. 02, Gaussian, Inc., Wallingford CT (2004).
11. G. Rauhut and P. Pulay, J. Phys. Chem. **99**, 3093 (1995).
12. J. Baker, A. A. Jarzecki, and P. Pulay, J. Phys. Chem. A **102**, 1412 (1998).
13. P. S. Anthony and L. Radom, J. Phys. Chem. **100**, 16502 (1996).
14. P. J. Stephens, F. J. Devlin, C. F. Chabalowshi, and M. J. Frish, J. Phys. Chem. **98**, 11623 (1994).
15. Y. Erdogdu and M. T. Gulluoğlu, Spectrochim. Acta A **74**, 162 (2009).
16. R. Ditchfield, Molecular Orbital Theory of Magnetic Shielding and Magnetic Susceptibility **56**, 5688 (1972).
17. K. Wolinski, J. F. Hinton, and P. Pulay, J. Am. Chem. Soc. **112**, 8251 (1990).
18. S. N. Azizi, A. A. Rostami, and A. Godarzian, J. Phys. Soc. Jpn. **74**, 1609 (2005).

19. C. M. M. Rohlfing, C. A. Leland, and R. Ditchfield, Chem. Phys. **87**, 9 (1984).
20. G. Keresztury, S. Holly, G. Besenyei, J. Varga, A. Wang, and J. R. Durig, Spectrochim. Acta A **49A**, 2007 (1993).
21. *Raman Spectroscopy: Theory, in Handbook of Vibrational Spectroscopy*, Ed. by G. Keresztury, J. M. Chalmers, and P. R. Griffith (Wiley, New York, 2002), Vol. 1.
22. C. Ogretir and S. Yarligan, J. Mol. Struc.-Theochem **425**, 249 (1998).
23. P. V. Maye and C. A. Venanzi, Struct. Chem. **1**, 517 (1990).
24. M. R. Hockridge, E. G. Robertson, and J. P. Simons, Chem. Phys. Lett. **302**, 538 (1999).
25. D. J. Nielsen, C. Pettinari, B. W. Selton, and A. H. White, Acta Crystallogr. C **60**, 542 (2004).
26. L. C. R. Andrade, J. A. Paixão, M. J. M. Almeida, M. A. C. Neves, and M. L. Sáe Melo, Acta Crystallogr. C **66**, 499 (2010).
27. E. D. Glendening, A. E. Reed, J. E. Carpenter, and F. Weinhold, NBO Version 3. 1, TCI, University of Wisconsin, Madison (1998).
28. C. James, C. Ravikumar,V. S. Jayakumar, and I. H. Joe, J. Raman Spectrosc. **40**, 537 (2009).
29. G. Socrates, *Infrared and Raman Characteristic Group Frequencies* (Wiley, Chichester, 2001).
30. N. Sundaraganesan, H. Saleem, and S. Mohan, Spectrochim. Acta A **59A**, 2511 (2003).
31. H. Saleem, A. R. Krishnan, Y. Erdogdu, S. Subashchandrabose, V. Thanikachalam, and G. Manikandan, J. Mol. Struct. **999**, 2 (2011).
32. Y. Erdogdu, M. T. Gulluoglu, and M. Kurt, J. Raman Spectrosc. **40** (11), 1615 (2009).
33. F. Billes, H. Endredi, and G. Jalsovszky, J. Mol. Struc. Theochem. **465**, 157 (1999).
34. S. Gunasekaran, S. R. Varadhan, and K. Manoharan, Asian J. Phys. **2** (3), 165 (1993).
35. H. O. Kalinowski, S. Berger, and S. Braun, *^{13}C NMR Spectroscopy* (Wiley, Chichester, 1988).
36. K. Pihlaja and E. Kleinpeter, *Carbon-13 Chemical Shifts in Structural and Stereo Chemical Analysis* (VCH Publishers, Deerfield Beach, 1994).
37. S. Sebastian, N. Sundaraganesan, B. Karthikeiyan, and V. Srinivasan, Spectrochim. Acta A **78**, 590 (2011).
38. S. Chandra, H. Saleem, Y. Erdogdu, S. Subashchandrabose, Akhil R. Krishnan, and M. T. Gulluoglu, J. Mol. Struc. **998**, 69 (2011).
39. T. Vijaykumar, I. H. Joe, C. P. R. Nair, and V. S. Jayakumar, Chem. Phys. **343**, 83 (2008).
40. K. Fukui, *Theory of Orientation and Stereo Selection* (Springer-Verlag, Berlin, 1975) (see also: K. Fukui, Science **218**, 747 (1987)).
41. D. F. V. Lewis, C. Ioannides, and D. V. Parke, Xenobiotica **24**, 401 (1994).